Remnants of Subdwarf Helium Donor Stars Ejected from Close Binaries with Thermonuclear Supernovae

Evan B. Bauer[1] , Christopher J. White[1], and Lars Bildsten[1,2]
[1] Kavli Institute for Theoretical Physics, University of California, Santa Barbara, CA 93106, USA; ebauer@kitp.ucsb.edu
[2] Department of Physics, University of California, Santa Barbara, CA 93106, USA

Abstract

Some binary systems composed of a white dwarf (WD) and a hot subdwarf (sdB) helium star will make contact within the helium burning lifetime of the sdB star. The accreted helium on the WD inevitably undergoes a thermonuclear instability, causing a detonation that is expected to transition into the WD core and lead to a thermonuclear supernova (SN) while the donor orbits nearby with high velocity. Motivated by the recent discovery of fast moving objects that occupy unusual locations on the HR diagram, we explore the impact of the thermonuclear SNe on the donors in this specific double detonation scenario. We use MESA to model the binary up to the moment of detonation, then 3D Athena++ to model the hydrodynamic interaction of the SN ejecta with the donor star, calculating the amount of mass that is stripped and the entropy deposited in the deep stellar interior by the strong shock that traverses it. We show that these donor remnants are ejected with velocities primarily set by their orbital speeds: 700–900 km s^{-1}. We model the long-term thermal evolution of remnants by introducing the shock entropy into MESA models. In response to this entropy change, donor remnants expand and brighten for timescales ranging from 10^6 to 10^8 yr, giving ample time for these runaway stars to be observed in their inflated state before they leave the galaxy. Even after surface layers are stripped, some donors retain enough mass to resume core helium burning and further delay fading for more than 10^8 yr.

1. Introduction

Recent observational and theoretical progress has revived the long considered double detonation scenario for thermonuclear supernova (SN; Nomoto 1982; Woosley & Weaver 1994; Livne & Arnett 1995), where a shell of accreted He detonates at a strength adequate to detonate the underlying carbon/oxygen (CO) white dwarf (WD). This totally disrupts the WD, with nucleosynthetic yields reflecting the WD core density (Fink et al. 2010; Sim et al. 2010; Shen et al. 2018b; Polin et al. 2019). For thin enough He shells, some (Kromer et al. 2010; Sim et al. 2010; Woosley & Kasen 2011; Shen et al. 2018b; Townsley et al. 2019) have argued that the diversity of SNe Ia may be explained by the range in the total WD mass (C/O core plus He shell) at the time of explosion. Thicker (approximately $>0.03 M_\odot$) He shells pose a challenge due to the predicted presence of heavy element ashes from the He detonation on the outer edges of the ejecta that are not seen in normal SNe Ia. Hence, binary scenarios that have lower mass He shells at the time of He detonation, such as the Am CVn systems (e.g., Bildsten et al. 2007) or dynamical mass transfer in a merger (Guillochon et al. 2010; Raskin et al. 2012; Pakmor et al. 2013; Moll et al. 2014; Tanikawa et al. 2015) remain the favored scenarios for double detonations as the cause of SNe Ia.

Although a rarer event than SNe Ia, the recent observation of De et al. (2019) of ZTF18aaqeasu (also referred to as SN 2018byg and ATLAS 18pqq) clearly showed the line blanketing indicative of heavy elements on the surface of the ejecta from a more massive He shell detonation that also triggered a core CO detonation. De et al.'s (2019) interpretation of the SNe spectra and light-curve led them to conclude that the He shell mass was $\approx 0.15 M_\odot$ on an underlying $0.75 M_\odot$ CO

WD, similar to the prediction of Bauer et al. (2017) for the explosive conditions reached in the future for the known galactic binary CD $-30°11223$ (Geier et al. 2013).

The binary scenario that naturally creates this explosive environment is a core He burning subdwarf (sdB) star of $M_1 < 0.5 M_\odot$ orbiting a CO WD (Iben & Tutukov 1991). Created in a common envelope event, these binaries are found in our Galaxy (Geier et al. 2013; Kupfer et al. 2017) and undergo gravitational wave losses on a timescale short enough (< 100 Myr) to initiate mass transfer while He is still burning in the core of the sdB star. Reaching contact at an orbital period of $P_{\rm orb} \approx 30$ minutes, the donor transfers helium to the companion WD at $\dot{M} \approx (2-3) \times 10^{-8} M_\odot$ yr^{-1} (Brooks et al. 2015; Bauer et al. 2017; Neunteufel et al. 2019). At these low $\dot{M}$'s, $\approx 0.05-0.25 M_\odot$ of He accumulates on the WD before it undergoes an unstable thermonuclear flash leading to the triggering He detonation (Brooks et al. 2015; Bauer et al. 2017).

At the time of the He (and presumably CO) detonation, the binary has an orbital period of 10–15 minutes. Depending on the WD mass, the whittled down $0.2-0.35 M_\odot$ donors have orbital velocities of $v_{\rm orb} \approx 600-900$ km s^{-1}. This velocity is naturally in the range of a set of recently discovered fast moving objects (Geier et al. 2015; Vennes et al. 2017; Raddi et al. 2018a, 2018b, 2019) that occupy an unusual part of the HR diagram between the main sequence and the WD cooling sequence. Motivated by this discovery, we explore here the impact of the resulting thermonuclear SNe on the donor for two specific scenarios that start with low-mass He burning star donors. Our 3D simulations yield mass stripping of the donor and the amount of entropy deposited in its deep interior due to the

Table 1
Donor Properties at the Moment the Accreted Helium Shell on the Companion Detonates

	Mass (M_1)	Radius (R_1)	Separation (a)	P_{orb}	v_{orb}	Accretor Mass (M_2)
Model 1	$0.344 M_\odot$	$0.080 R_\odot$	$0.271 R_\odot$	20.8 minutes	691 km s^{-1}	$0.927 M_\odot$
Model 2	$0.233 M_\odot$	$0.041 R_\odot$	$0.147 R_\odot$	9.4 minutes	882 km s^{-1}	$0.779 M_\odot$
	ρ_c (g cm^{-3})	T_c (K)	p_c (dyne cm^{-2})	$p_c/n_c\, k_B\, T_c$	$\langle p \rangle / \langle n k_B T \rangle$	
Model 1	3.74×10^4	1.10×10^8	2.83×10^{20}	1.23	1.21	
Model 2	6.71×10^4	7.49×10^7	4.55×10^{20}	1.73	1.56	

Note. Angle brackets denote mass-averaged quantities, such as mass-averaged pressure $\langle p \rangle \equiv \int p\, dm / M$.

shock from the ejecta sweeping across it. We then explore the subsequent longer-timescale expansion and brightening of the donor over thermal timescales and place these shock-heated donors on the HR diagram. Some of our scenarios yield objects close to those observed. We do not address the much higher velocity (up to ≈ 2000 km s^{-1}) objects found by Shen et al. (2018a), as the He core burning donor scenarios cannot reach such compact orbital configurations.

2. MESA Models of He Star Donors

We construct two models of sdB He stars that donate material to WD binary companions using the binary evolution capabilities of MESA (Paxton et al. 2011, 2013, 2015, 2018, 2019). All MESA models use release version 10398. Our methods closely follow those of Brooks et al. (2015) and Bauer et al. (2017), including the $^{14}N(e^-, \nu)^{14}C(\alpha, \gamma)^{18}O$ (NCO) reaction chain that triggers He shell ignition in the accreting WD. We employ the rates adopted in Bauer et al. (2017) for these reactions.

Model 1 is based on the observed system CD $-30°11223$ (Geier et al. 2013), which consists of a $M_1 = 0.51 M_\odot$ He core burning star with a $M_2 = 0.762 M_\odot$ WD companion in a 70.5 minute orbital period. Our MESA binary model predicts that gravitational wave radiation will bring this system into contact in 37 Myr while the donor is still burning helium in its core and the orbital period is 33 minutes. Over 10 Myr, the donor transfers $0.17 M_\odot$ of He-rich material to the WD, triggering a He shell detonation when $P_{orb} = 20.8$ minutes. Such an event likely causes a SN similar to ZTF 18aaqeasu (SN 2018byg, De et al. 2019). Our binary model for this system is very similar to that of Brooks et al. (2015) with the accretor modeled as in Bauer et al. (2017). The only major difference is that for the He core burning donor model we employ the predictive mixing scheme described in Paxton et al. (2018) for locating the convective boundary during core helium burning, resulting in a more extended core and 120 Myr core helium burning lifetime. Changes to the binary mass transfer are negligible, but the predictive mixing scheme does change the interior profile of the donor at the moment of the companion explosion.

Model 2 explores the possibility of a low-mass He core burning star that donates more mass before the WD explodes. This scenario has a more compact orbit with higher orbital velocity at the time of explosion, and the potential for the donor to be more impacted by the SN ejecta. Model 2 consists of a $M_1 = 0.46 M_\odot$ He core burning star with a $M_2 = 0.55 M_\odot$ WD that we initialize with a 70 minute orbital period. After coming into contact at $P_{orb} = 33$ minutes, the donor transfers $0.23 M_\odot$ of He-rich material before the accumulated shell ignites on the accreting WD when $P_{orb} = 9.4$ minutes. Due to the donor

losing enough mass to fall below $0.3 M_\odot$, nuclear burning has ceased in its core (Brooks et al. 2015). However, the donor's adiabatic response to ongoing mass loss prevents it from contracting and causes mass transfer to continue even after burning ceases.

Table 1 shows the final properties of the two MESA donor models at the moment of He shell ignition on the companion WD, which we presume corresponds to an SN soon thereafter.

For a Roche-lobe filling donor of mass M_1 in a system with mass ratio $q = M_1/M_2 \approx 1/3$, the Eggleton (1983) formula gives the ratio of the donor radius R_1 to the orbital separation a as

$$\frac{R_1}{a} = \frac{0.49 q^{2/3}}{0.6 q^{2/3} + \ln(1 + q^{1/3})} \approx 0.3. \quad (1)$$

This shows that values of the ratio R_1/a similar to those seen in Table 1 are generic for the sdB+WD binary evolution scenario at the time of explosion. The spatial velocity of the donor is

$$v_{orb}^2 = \frac{GM_2}{a(1 + q)}. \quad (2)$$

Combining this with Equation (1), the radius of the donor at the time of explosion can be expressed in terms of its orbital velocity as

$$R_1 \approx \frac{0.3}{1 + q} \frac{GM_2}{v_{orb}^2} \approx 0.04\, R_\odot \left(\frac{M_2}{M_\odot} \right) \left(\frac{1000 \text{ km s}^{-1}}{v_{orb}} \right)^2. \quad (3)$$

Invoking orbital motion to explain high-velocity objects therefore requires compact radii. For high-velocity objects such as those found by Raddi et al. (2018a, 2018b, 2019), their current position on the HR diagram indicates that they must have expanded in radius since the explosion for a binary evolution scenario to be a viable explanation of observed velocities. For the even higher velocity (up to ≈ 2000 km s^{-1}) objects of Shen et al. (2018a), Equation (3) indicates they must have had $R \approx 0.01 R_\odot$ at the moment of explosion, requiring even more significant inflation to achieve their currently observed states.

Equation (1) also indicates that the fraction of the solid angle surrounding the exploding WD filled by the donor is $\pi R_1^2 / 4\pi a^2 = (R_1/a)^2/4 \approx 0.02$. The total binding energy of the donor remnants is $(2-4) \times 10^{48}$ erg. So for an explosion resulting in ejecta with a total energy of $\approx 10^{51}$ erg, the ejecta that intersect the donor remnant contain sufficient energy to have an impact on its binding energy and radius, or to unbind significant amounts of mass from the star, as we now explore.

3. Estimating the Shock Strength in the Donor

Though none have calculated the specific binary scenario we are exploring here, there has been substantial prior work on SNe ejecta sweeping across nearby companions, both from thermonuclear and core collapse events (Wheeler et al. 1975; Taam & Fryxell 1984; Marietta et al. 2000; Pan et al. 2010, 2012a, 2012b, 2013; Liu et al. 2013; Hirai et al. 2014, 2018). The focus of much of these earlier efforts was on understanding the mass stripped from the donor and the resulting kick. Closer to our case, previous studies have examined the interaction of SN Ia ejecta with He-star companions (Pan et al. 2010, 2012b, 2013; Liu et al. 2013), especially with regard to how much mass can be stripped from the star. Pan et al. (2012a, 2013) also explored post-impact thermal evolution of the donor using MESA models. As shown by Pan et al. (2014), deeply injected entropy allowed the remaining shocked donor to stay hot (and potentially visible) for hundreds of years after the SNe event. These, however, were for He-star companions with masses in the range 0.7–1.2 $M_\odot$, much larger than the $\approx 0.3\,M_\odot$ remnants that we study here. As we show, the lower masses of our systems enable a much more prolonged bright phase after the thermonuclear event.

Though we will investigate mass loss and kicks from the ejecta momentum, we want to emphasize here the thermal impact on the donor of the shock that traverses its core. As the entropy jump associated with the deeply penetrating shock wave depends on the shock pressure versus that in the ambient star, we start by estimating the ejecta pressure at the location of the donor,

$$p_{\rm ej} \approx \frac{M_2 v_{\rm ej}^2/2}{4\pi a^3/3}, \qquad (4)$$

where $v_{\rm ej}$ is the mass-averaged ejecta velocity. When the donor is well characterized as an $n = 3/2$ polytrope, its central pressure is $p_{\rm c,p} = 0.77 GM_l^2/R_l^4$. Assuming that the donor is also Roche-lobe filling then yields the ratio

$$\frac{p_{\rm ej}}{p_{\rm c,p}} \approx \frac{7 \times 10^{-3}}{q^{2/3}(1+q)^{7/3}} \left(\frac{v_{\rm ej}}{v_{\rm orb}}\right)^2. \qquad (5)$$

This equation's prime value is in the scaling that indicates a much larger impact on the entropy for the widest Roche-lobe filling binaries. An excellent case of this is shown by Taam & Fryxell (1984) where a much wider binary polytropic companion suffers a very large central pressure perturbation. It is also evident in Marietta et al.'s (2000) work on a model of a near solar analog star (their model HCV) in a $\approx 9.75\,{\rm hr}$ Roche-lobe filling orbit around a $M_2 = 1.378 M_\odot$ WD. In their case, $v_{\rm orb} \approx 230\,{\rm km\,s}^{-1}$, and Equation (5) predicts $p_{\rm ej}/p_{\rm c,p} \approx 2$ for their ejecta model. This was explicitly noted by Marietta et al. (2000) as they diagnosed the outcome of their simulation. The later simulations by Pan et al. (2012a, 2012b, 2013) also exhibited substantial interior thermal perturbations.

If our donors were simple $n = 3/2$ polytropes, then Equation (5) would imply that $p_{\rm ej}/p_{\rm c,p} \approx 0.3$ for $v_{\rm ej} = 5000\,{\rm km\,s}^{-1}$ certainly indicating the need to perform the rigorous 3D calculation that follows. However, having undergone substantial burning that modifies their compositions throughout, as well as having internal entropy gradients, our donors are far from

polytropes. Despite that, we can use the values in Table 1 to make a few preliminary estimates. Model 1 has a central pressure about a factor of 10 larger than an $n = 3/2$ polytrope, whereas Model 2 is about a factor of three higher in central pressure than a polytrope. The resulting values of $p_{\rm ej}/p_{\rm c}$ for a 10^{51} erg explosion are 0.1 for Model 1 and 0.5 for Model 2. It is also important to note that the volume averaged pressure in a stellar model is $\langle p \rangle = -2E_{\rm tot}/3V$ where V is the volume of the star and $E_{\rm tot}$ is its total energy. Hence for a 10^{51} erg explosion, Model 1 ($E_{\rm tot} = -4.2 \times 10^{48}$ erg) has $p_{\rm ej}/\langle p \rangle \approx 9$, while Model 2 ($E_{\rm tot} = -2.6 \times 10^{48}$ erg) has $p_{\rm ej}/\langle p \rangle \approx 12$. Hence, for both cases a very large part of the donor's volume (though maybe not its mass) will undergo a strong shock. As we will see, this leads to mass loss at different levels.

4. Ejecta–Donor Interaction Computations

The density and pressure profiles of the two MESA models are used to initialize 3D Athena++ models on 256^3 grids. Model 1 has an initial diameter of 46 cells on its grid, while Model 2 has a diameter of 45 cells. As the donor stars are nearly nondegenerate (as indicated in Table 1) Athena++ is run with $\Gamma = 5/3$ ideal hydrodynamics and with self-gravity based on the fast Fourier transform. The initial stars are allowed to settle into numerical hydrostatic equilibrium on these new grids for 30 characteristic dynamical times $t_{\rm dyn} = \sqrt{5/8\pi G\rho_{\rm c}}$ (totaling 270 s and 200 s, respectively) before interacting with the modeled ejecta. Though the resolution used is not sufficient to fully resolve the tenuous stellar atmosphere, the stars quickly find this new equilibrium, which is very similar to the MESA model throughout the interior (see Section 5 for more detail).

For the ejecta, we use the model presented in Kasen (2010) with power-law slopes $\delta = 1$ and $n = 10$, truncated to have velocity less than $20{,}000\,{\rm km\,s}^{-1}$. The ejecta mass is set to be the accretor mass at explosion, and the ejecta kinetic energy is set to be 0.2, 0.5, 0.7, or 1.0×10^{51} erg. These kinetic energies are chosen to explore the range of possible outcomes. The corresponding mass-averaged ejecta velocities span the ranges $v_{\rm ej} = 4330$–$9740\,{\rm km\,s}^{-1}$ (Model 1) and $v_{\rm ej} = 4720$–$10{,}600\,{\rm km\,s}^{-1}$ (Model 2). To account for the losses from adiabatic expansion of the ejecta's internal energy from the time of explosion, we set the internal energy density of the ejecta to be proportional to $1/t$ times the kinetic energy density when it enters the grid at time t after explosion. The normalization is such that $10{,}000\,{\rm km\,s}^{-1}$ ejecta will have an internal energy 7%–9% of its kinetic energy when it reaches the donor. When incorporating the ejecta into the 3D simulation, we shift the velocities to account for the relative orbital motion between the donor and accretor.

Figure 1 shows the density in the orbital plane for two of the 3D Athena++ computations with Model 1, each 100 s after explosion. The WD accretor is located off the domain, $0.2706 R_\odot$ to the left of the origin, with the donor's orbital velocity in the positive y-direction. The left panel shows the 0.2×10^{51} erg case, while the right panel shows the 1.0×10^{51} erg case. Figure 2 shows the same density slices for Model 2, also 10 s after explosion. In this case, the WD accretor is $0.147 R_\odot$ to the left of the origin.

As noted earlier, when hit with the ejecta, a strong shock passes through the donor, inducing a series of pulsations that decay over many dynamical times. This can be seen in the top panels of Figure 3, which show the time evolution of the central density normalized by the central density of the MESA model given to Athena++. The central pressure is
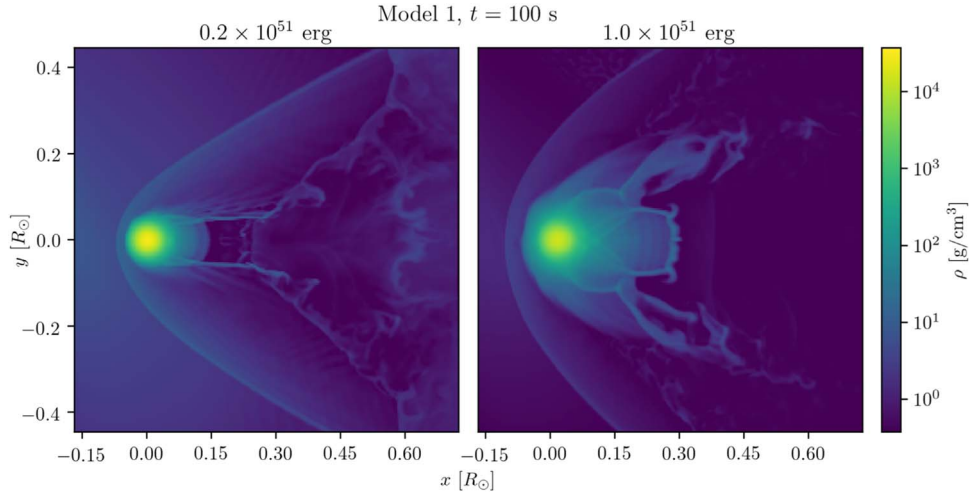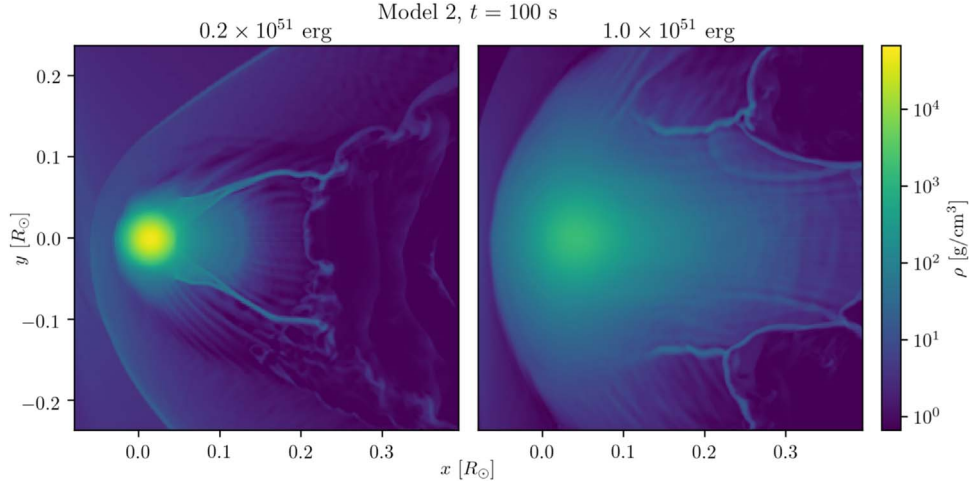
Figure 1. Density in two simulations of ejecta interacting with Model 1. The lowest ejecta energy is on the left, with the highest on the right. Both snapshots are taken 100 s after explosion. The animation shows time evolution of this density over the entire simulation. Animations for each of the `Athena++` models presented in this work are available at doi:10.5281/zenodo.3479926.

(An animation of this figure is available.)

Figure 2. Density in two simulations of ejecta interacting with Model 2. The lowest ejecta energy is on the left, with the highest on the right. Both snapshots are taken 100 s after explosion. The animation shows time evolution of this density over the entire simulation.

(An animation of this figure is available.)

qualitatively the same. The initial spikes in the central density increase with explosion energy, as expected.

In the 3D computations we define the extent of the star at any time using the following approach. Given the center of mass, we construct spherically averaged radial profiles of the Bernoulli parameter

$$\mathrm{Be} \equiv \frac{1}{2}v^2 + \frac{\Gamma}{\Gamma - 1}\left(\frac{p}{\rho}\right) + \Phi, \qquad (6)$$

where v is the velocity measured relative to the star's bulk motion and Φ is the gravitational potential relative to 0 at infinity. We take the edge of the star to be the innermost radius where the Bernoulli parameter vanishes. The results do not change much if we use total specific energy $\mathrm{Be} - p/\rho$ instead, though the Bernoulli parameter properly accounts for a fluid element being able to reach infinity using not just its kinetic

energy and, via cooling, its internal energy, but also using its pressure via expansion into vacuum. With this definition, we can measure the radial extent and total bound mass of the donor as a function of time as plotted in Figure 3. While these radii do sometimes exceed the initial distance between the donor's center and the edge of the grid, kicks provided by the ejecta move the donor sufficiently far from the edge for the bound material to never leave the grid in any case.

The donors' outer radii dramatically increase after interacting with the ejecta, especially in the higher-energy explosions. This occurs for two reasons. The first reason is the expected hydrostatic expansion of a star due to rapid mass loss, while the second reason is the increase in entropy deep in the star due to the shock wave traversal. As we show later, the amount and location of this deposition of heat will determine the appearance of the star at much later times. We show the effect of the shock wave traversal by plotting the spherically averaged
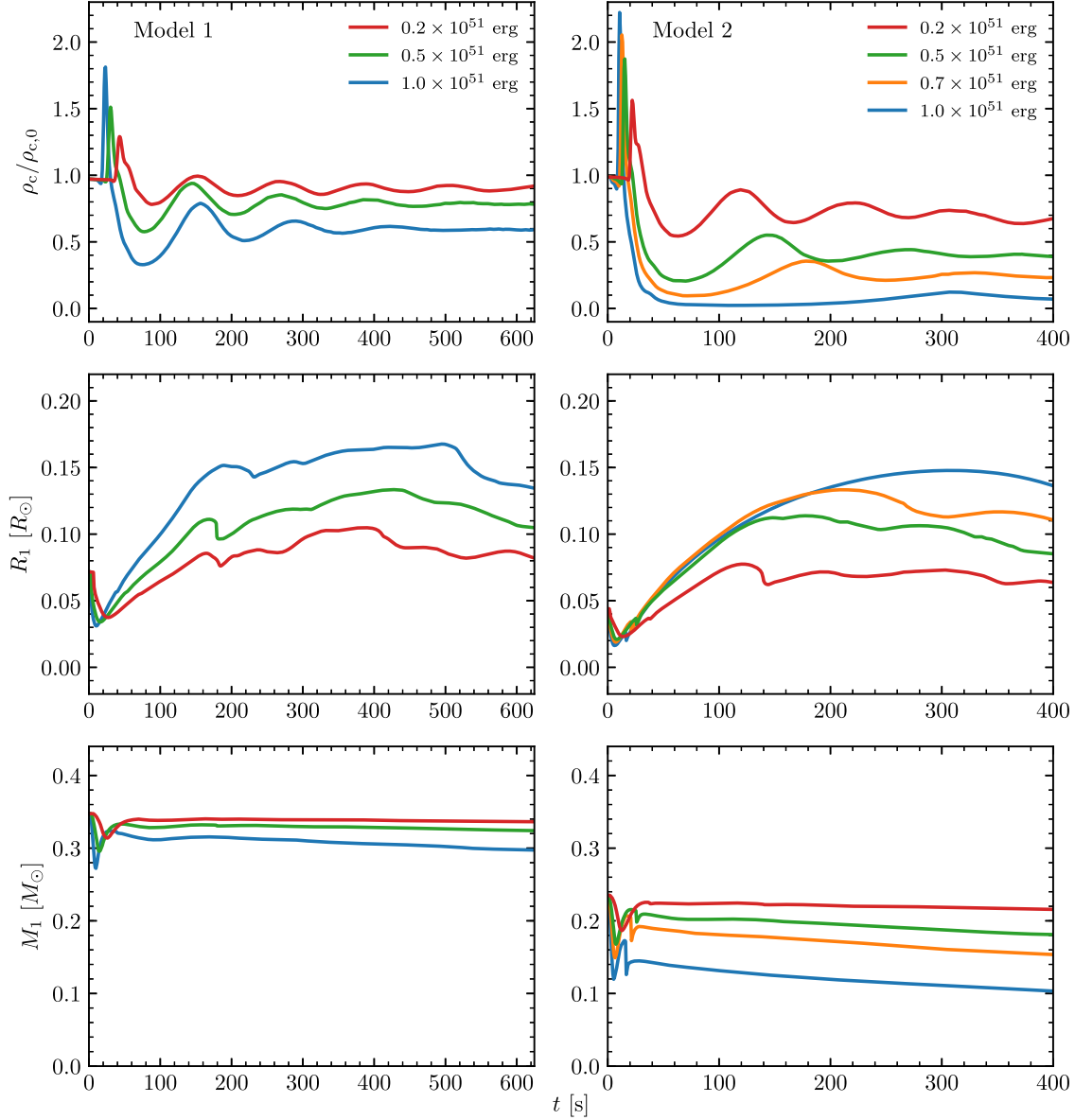
Figure 3. Central density, radius, and bound mass of the two donors as functions of time after explosion. Larger kinetic energies in the ejecta cause stronger oscillations and increase the radii more, while also stripping more mass.

profiles of entropy per unit mass relative to the initial central value,

$$s \equiv \frac{k_{\mathrm{B}}}{(\Gamma - 1)\mu m_{\mathrm{p}}} \log\left(\frac{p}{\rho^{\Gamma}} \frac{\rho_{\mathrm{c},0}^{\Gamma}}{p_{\mathrm{c},0}}\right), \qquad (7)$$

where k_{B} is Boltzmann's constant, μ is the mean molecular weight, and m_{p} is the baryon mass. Figure 4 shows the initial entropy profiles, as well as the profiles at the end of the 3D simulations, 70 dynamical times after the explosion. The substantial entropy gradient in the initial models helps to explain why our polytropic estimates for central pressures were not accurate. The large increase in entropy in the outermost layers reflect the much stronger shocks that can be achieved at the lower pressures there.

Table 2 summarizes the outcomes of the seven 3D hydrodynamical models, labeled by the initial 1D model number and the kinetic energy of the explosion. The final bound remnant always has a mass less than the initial donor mass. The density floor used in the modeling is 10^{-5} the initial central density. As a result this floor material will only have a mass 0.04% (0.01%) that of the initial Model 1 (Model 2) donor in an equal volume, and it will comprise a mass of 13% (5%) that of the initial donor over the entire simulation volume.

We define the change in average entropy per unit mass using the initial and final entropy profiles:

$$\Delta s_{\mathrm{ave}} = \frac{1}{M_{\mathrm{f}}} \int_0^{M_{\mathrm{f}}} (s_{\mathrm{f}} - s_{\mathrm{i}}) \, dm. \qquad (8)$$

This increases with increasing explosion energy, as expected. We also report Δs_{c}, the change in entropy per unit mass at the center of the donor, as well as the fractional changes in central density and pressure.

Table 2
Summary of 3D Modeling

Model	M_f $(M_\odot)$	Δs_{ave} $(k_B/\mu m_p)$	Δs_c $(k_B/\mu m_p)$	$\rho_{c,f}/\rho_{c,i}$	$p_{c,f}/p_{c,i}$	v_{kick} (km s^{-1})	v_f (km s^{-1})	$4\pi I_{kick}/\Omega_x I_{ej}$
1:0.2	0.336	0.077	0.00	0.95	0.91	52	680	0.19
1:0.5	0.324	0.21	0.012	0.80	0.70	120	700	0.28
1:1.0	0.297	0.40	0.034	0.61	0.45	180	710	0.28
2:0.2	0.214	0.20	0.11	0.70	0.60	150	880	0.44
2:0.5	0.178	0.50	0.33	0.37	0.24	270	920	0.42
2:0.7	0.150	0.63	0.19	0.25	0.11	310	930	0.34
2:1.0	0.0952	0.93	0.17	0.076	0.015	330	940	0.19

Note. Models are labeled according to donor model number and the kinetic energy of the explosion in units of 10^{51} erg.
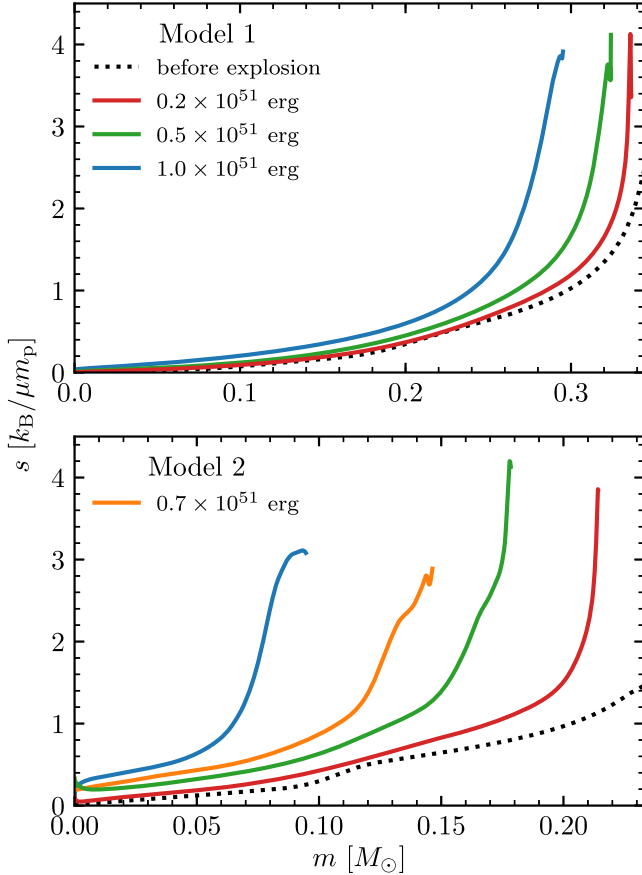

Figure 4. Entropy profiles for the two models, before and after interacting with the supernova.

The explosion delivers an impulse to the donor over a relatively short time, after which the donor coasts at a well-defined kick velocity v_{kick} for the remainder of the simulation. These velocities, calculated in the initial rest frame of the donor, are dominated by the component in the x-direction in the sense of Figures 1 and 2. Due to the drag on the donor moving through the ejecta (from its orbital motion), there is also a slight negative component in the y-direction, which becomes more important at lower ejecta velocities, but it only ranges over 3–13 km s^{-1} across all simulations. Though v_{kick} can be a nonnegligible fraction of v_{orb}, the two are largely orthogonal and the latter dominates the final velocity v_f of the donor relative to the binary barycenter. In fact, in some cases the small drag in the negative y-direction leads to a reduced final barycentric velocity, despite the kick in the x-direction. These velocities are reported in Table 2.

The final column of Table 2 measures the fraction of ejecta momentum intercepting the donor that contributes to the final velocity. That is, we measure the kick impulse

$$I_{kick} = M_f v_{kick}^x, \qquad (9)$$

and compare it to the total impulse in the ejecta model

$$I_{ej} = \int_0^{M_{ej}} v_{ej}\, dm_{ej}. \qquad (10)$$

The latter must be scaled by the cross section to the explosion presented by the donor, with each line of sight weighted by the ratio of the ejecta x-momentum to the total ejecta momentum. The resulting scale factor is $\Omega_x/4\pi$, where $\Omega_x = \pi R^2/a^2$. The resulting values are less than unity, indicating some x-momentum in the ejecta is deflected around the star. We expect this to be the case, given that the ejecta has a finite Mach number and forms a visible bow shock when interacting with the donor. For Model 2, much of the momentum lost by the ejecta in the highest energy explosions goes toward accelerating ultimately unbound material, resulting in low intercepted momentum fractions for the bound remnant. In all of our cases, we find that $4\pi I_{kick}/\Omega_x I_{ej}$ is in the range of $1/3$ noted by Hirai et al. (2018).

While the modeling here only considers ejecta from a nonrotating accretor, little would change with the addition of rotation. The accretor surface breakup velocities at the time of explosion are 4300 and 3400 km s^{-1} for Models 1 and 2, respectively. Even if all the ejecta were moving this rapidly in the tangential direction at explosion, the tangential velocities at the location of the donor would be reduced by the ratio of the separation to the accretor radius, resulting in 150 and 300 km s^{-1}. These values are 16% and 26% of the y-velocities already seen due to the orbital motion. This would slightly modify the 3–13 km s^{-1} impact on the donor velocities due to drag, and in fact prograde motion would operate to reduce this already small drag effect.

5. Post-interaction Evolution with MESA

After the oscillations in the bound remnants have died away (see Figure 3), we record shellular averages of the Lagrangian change $\Delta \ln(p/\rho^\Gamma)$ from the Athena++ models for fluid elements in the remaining stellar interior. The profile for the local entropy change is then given by

$$\Delta s \equiv \frac{3}{2}\frac{k_B}{\mu m_p}\Delta \ln\left(\frac{p}{\rho^\Gamma}\right), \qquad (11)$$

which we inject over an arbitrary time interval Δt into the `MESA` donor models as a local heating term

$$\epsilon_{\text{heat}} = T \frac{\Delta s}{\Delta t} , \qquad (12)$$

where T is the local temperature. During the entropy injection phase, we set the model timesteps to be about one second over a typical time interval $\Delta t = 100$ s, after which heating shuts off and we begin tracking the subsequent thermal evolution. The $\Delta t \approx 100$ s is long enough so that the star can hydrostatically readjust. The temperature change due to this heating is

$$\frac{\Delta T}{T} = \frac{\Delta s}{c_V} , \qquad (13)$$

where $c_V \approx (3/2)k_B/\mu m_p$ is the specific heat capacity at constant volume. This implies that profiles of relative temperature change can be inferred from the differences between the dashed and solid curves in Figure 4. After injecting these entropy changes over the interior mass that remains bound in each model, we also strip mass from the surface of the `MESA` model to match the final bound mass seen in the `Athena++` runs (Table 2). We remove mass using the `MESA` option `relax_mass` with a mass loss rate of 10^{-4} $M_\odot$ yr^{-1}. This relaxation procedure removes mass adiabatically and performs pseudo-evolution to reconverge to hydrostatic equilibrium while suppressing any composition changes due to mixing or nuclear burning. The timescales for mass stripping are on the order of 10^3 yr or less, so transient behavior on shorter timescales than this due to thermal readjustment near the surface in the `MESA` models should be ignored. The remainder of this section focuses on the structure changes due to entropy injection in deeper layers, where we show that thermal adjustment timescales are longer than the mass stripping timescale. The entropy profile stays nearly constant in these layers during mass stripping.

Figure 5 shows the change in binding energy from this procedure, and compares the energy profiles in the `MESA` model to the energy profiles from the `Athena++` run. The "preshock" `Athena++` profiles are shown after the models have settled into hydrostatic equilibrium on the `Athena++` grid, demonstrating that although there are small changes due to different equation-of-state treatments when initializing the `MESA` progenitor model into the `Athena++` simulation, the differences are small enough that we can still resolve the changes in the bulk structure due to the shock that traverses the donor star. The evident agreement of post-shock models in Figure 5 verifies that our procedure for adjusting the `MESA` model accurately captures the change in binding energy from the ejecta interaction modeled with `Athena++`.

The models will then thermally respond to the new entropy profiles. The heating of the interior results in inflation to larger radii, analogous to the thermal wave described by Zhang et al. (2019) for WDs with entropy deposited in the interior by nuclear heating. Figure 6 shows the long-term radius evolution for models 1 and 2. The timescale for the initial radius expansion and brightening is set by the local heat diffusion timescale at the location of peak heating,

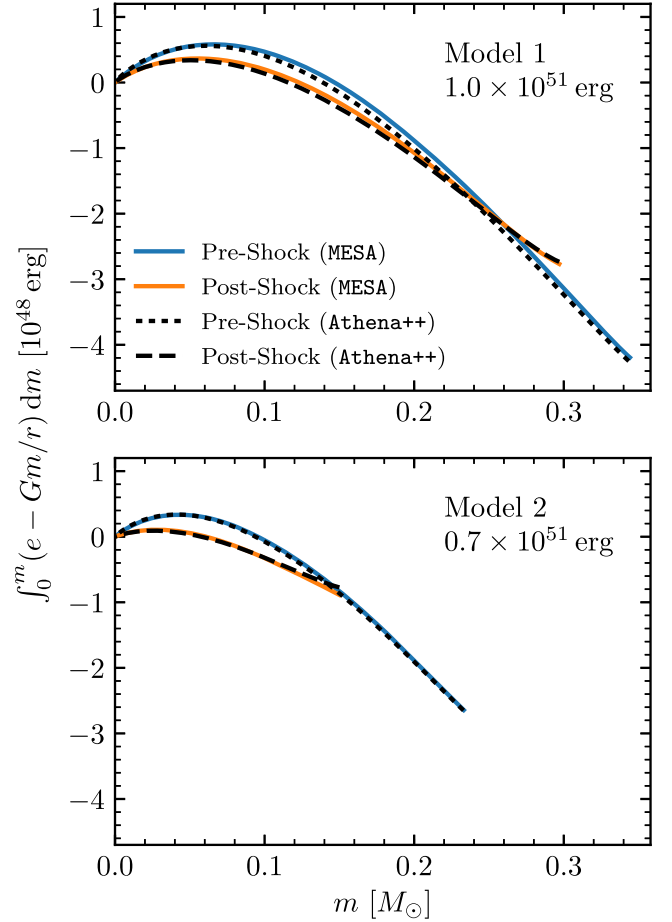$$t_{\text{th}} = \frac{H^2}{D_{\text{th}}} , \qquad (14)$$

Figure 5. Integrated energy profiles (thermal + potential) showing the overall change in binding energy after the shock from the supernova ejecta deposits entropy and strips mass from the surface.

where $H = P/\rho g$ is the local pressure scale height and $D_{\text{th}} = 4acT^3/3\kappa\rho^2 c_P$ is the thermal diffusion coefficient. For a Kramers opacity ($\kappa \propto T^{-3.5}$), this timescale depends strongly on temperature: $t_{\text{th}} \propto T^{-6.5}$.

Figure 7 shows the profiles for total heating in the interior of each remnant model along with interior profiles of t_{th} at the end of the heat injection phase. The timescale for radius expansion seen in Figure 6 corresponds to the value of t_{th} at the location of peak heating seen in Figure 7. Note that even though the initial thermal diffusion timescale in layers exterior to the peak heating location can be longer, the thermal wave propagating through them heats and adjusts the structure of these layers as it reaches them, significantly reducing the timescale for heat transport (Zhang et al. 2019). It is therefore only the local thermal time for the wave to begin propagating that sets the timescale for its emergence from the star. Note that although Table 1 shows that the core pressure of model 2 is somewhat nonideal due to the onset of electron degeneracy, Figures 4 and 7 show that the most important layers for entropy and heat deposition lie toward the surface of the star, where conditions are much closer to ideal gas. Effects of a nonideal equation-of-state in the `Athena++` models for donor stars will be a subject of future work, but we do not expect significant changes for the sdB donor stars presented in this work.
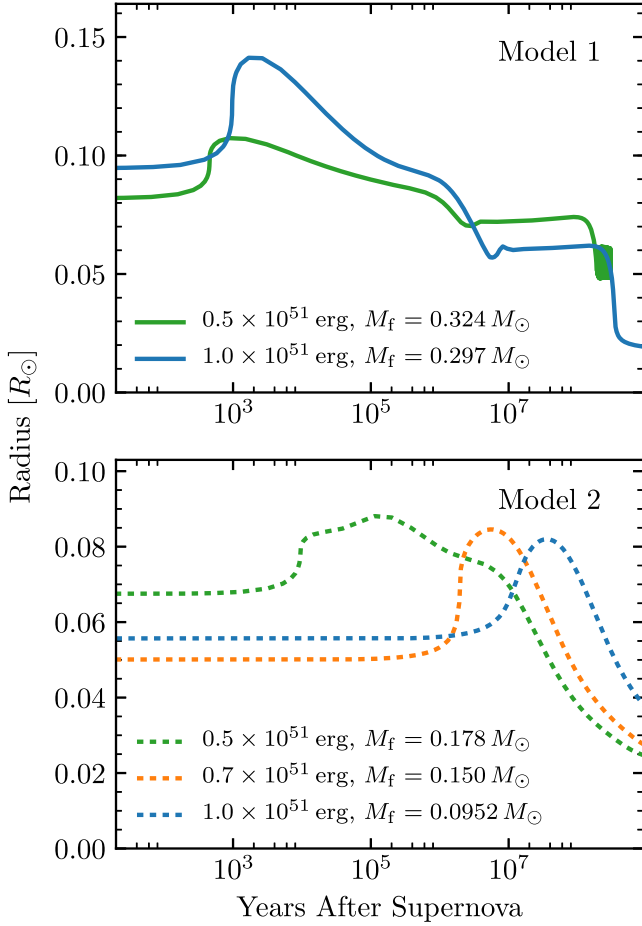
Figure 6. Long-term radius evolution of `MESA` models after introducing the entropy change from ejecta interaction in the `Athena++` models. The labels for each line correspond to the total kinetic energy of the ejecta in the `Athena ++` run. Note that we omit the two cases with the lowest energy explosions (0.2×10^{51} erg) from this and subsequent figures to improve clarity and because the lowest ejecta energies have only superficial impact for short timescales.

Figure 7. Upper panel: profiles of the local heat diffusion timescale (Equation (14)) in the `MESA` models for the remnants immediately following entropy injection. Lower panel: profiles of the total heating introduced into the `MESA` remnant models by the procedure described in Equations (11) and (12).

The expansion and increased luminosity persist over the Kelvin–Helmholtz timescale $t_{KH} \sim GM^2/RL$, which ranges from 10^5 to 10^8 yr depending on the luminosity L after the thermal wave has reached the surface of the donor remnant. The trend is for the overall duration of the brightening event to be shorter for more massive remnants due to higher peak luminosity. This trend is also consistent with the results of Pan et al. (2013), whose models exhibit similar brightening events but with much shorter duration (10–100 yr) for their more massive (0.7–$1.2 M_\odot$) He-star companion models that brightened to 10^3–$10^4 L_\odot$.

The entropy deposited in the core of model 1 initially reduces the density and temperature there, temporarily halting core helium burning, but because $M_2 > 0.3 M_\odot$, these models eventually contract enough to resume core He burning and achieve a fixed radius and luminosity lasting ≈ 100 Myr, thus making an unusually low-mass He core burning star. For model 2, the timescale is much longer (up to 10^8 yr) due to the much lower remnant luminosity. After their initial phase of radius expansion, the remnants from model 2 cool and contract as low-mass WDs incapable of any further nuclear burning.
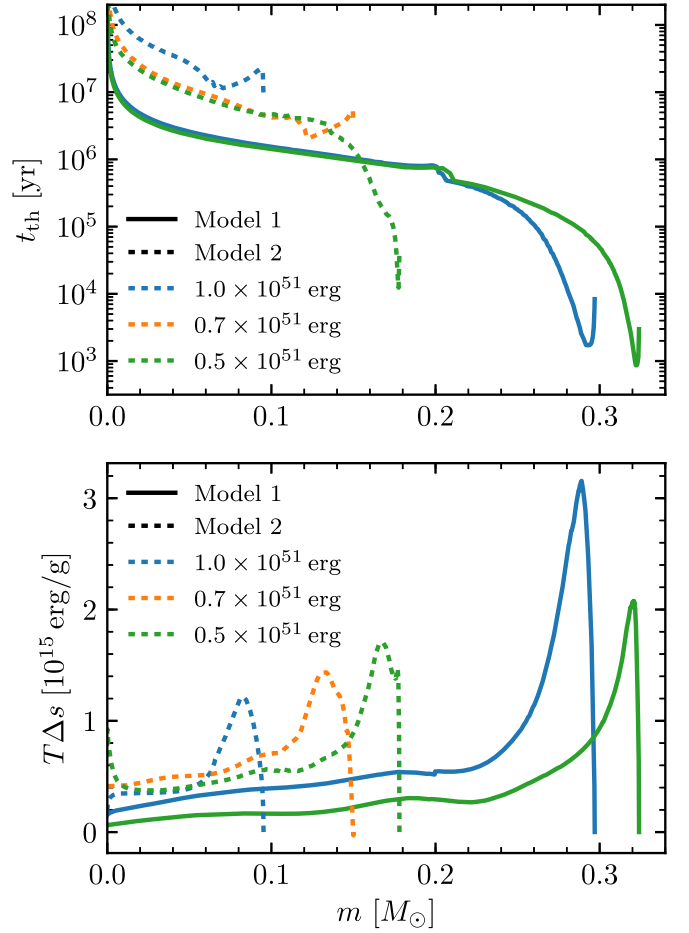
Figure 8 compares the model HR diagram tracks to a few high-velocity objects. Notably, with the right ejecta energy, model 2 can evolve near the locations on the HR diagram for GD 492 (LP 40–365) and J1603–6613 (Vennes et al. 2017; Raddi et al. 2018a, 2018b, 2019), and remain there for the 10^6–10^7 yr expected from their kinematics and location in the galaxy. The ejection velocities for our models are somewhat higher than the ≈ 600 km s^{-1} inferred by Raddi et al. (2018a, 2019) for these objects when accounting for the rotation velocity of the galactic disk.

We also include an estimated point for US 708 using the values of T_{eff} and $\log g$ given by Geier et al. (2015), where $L = 4\pi R^2 \sigma_{SB} T_{eff}^4$ and we estimate R using the measured $\log g$ and assuming that $M \approx 0.3 M_\odot$. Our track for model 1 suggests that a more massive object is needed to achieve the higher temperature and luminosity of US 708, though in this case it may be difficult for the binary system to achieve a compact enough orbit to explain the high velocity of US 708. However, Brown et al. (2015) have noted that the higher velocity of US 708 could be explained if it originated from a binary in the stellar halo traveling at ≈ 400 km s^{-1} in the same direction that the remnant is ejected from the binary.

Table 3
Rotational Properties of Donor Remnants 10 Myr after Explosion

Model	$P_{rot,0}$ (minutes)	Case 1 (See Text)			Case 2 (See Text)		
		P_{rot} (minutes)	$\Omega_{rot}/\Omega_{crit}$	v_{rot} (km s^{-1})	P_{rot} (minutes)	$\Omega_{rot}/\Omega_{crit}$	v_{rot} (km s^{-1})
1:0.5	20.8	61	0.094	86	20	0.28	261
1:1.0	20.8	52	0.080	80	17	0.25	249
2:0.5	9.4	61	0.093	71	14	0.40	301
2:0.7	9.4	161	0.064	38	28	0.37	219
2:1.0	9.4	230	0.048	24	62	0.18	88
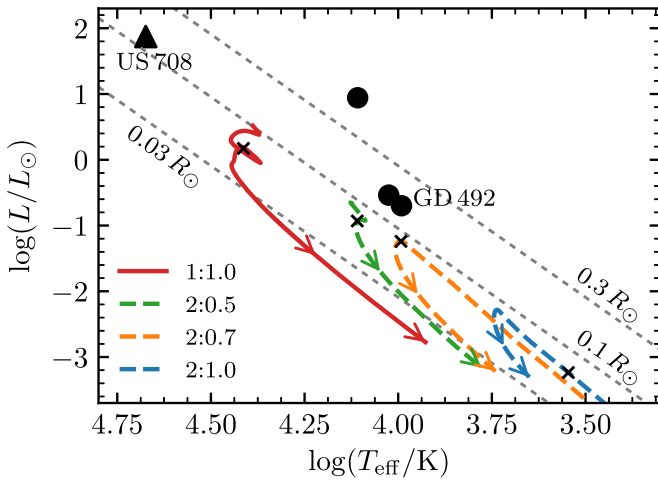
Figure 8. HR diagram. Tracks are labeled as the corresponding models in Table 2 and begin 10^5 yr after the companion explosion to avoid showing early portions of evolution that are unlikely to be observed. A black x marks the point 10^7 yr after the companion explosion on each track. The three circles show high-velocity objects of Raddi et al. (2019), including GD 492.

6. Conclusions and Future Work

We have modeled WD+sdB binary star systems and shown that the donor sdB stars can be expected to become unusual runaway stars with velocities of 600–900 km s^{-1}. The onset of mass transfer in these binary systems occurs at $P_{orb} \approx$ 30 minutes, when a $0.46 M_\odot$ star fills the Roche lobe while still burning He in its core. For a massive ($\approx 1.0 M_\odot$) and hot accreting WD, a shell detonation can occur after the system has transferred only a few hundredths of a solar mass of He (Brooks et al. 2015; Bauer et al. 2017), with the donor orbital velocity $v_{orb} \approx 600$ km s^{-1}. In contrast, our $0.55 M_\odot$ accreting WD model accumulates a much larger ($0.23 M_\odot$) He envelope before igniting when $P_{orb} = 9.4$ minutes, while the donor has a much higher orbital velocity of $v_{orb} = 880$ km s^{-1}. These two cases provide an estimate of the dynamic range in final velocities from this scenario.

Depending on the orientation of ejection velocity v_f relative to the system's prior orbit within the galaxy, objects with $v_f \lesssim 800$ km s^{-1} may either escape the galaxy or remain bound in unusual galactic orbits (for initial galactic disk orbits of 250 km s^{-1} and galactic escape velocity 550 km s^{-1}, Raddi et al. 2019). Based on their trajectories from the galactic midplane, and under the assumption that the objects they observed are young ($\leqslant 10$ Myr), Raddi et al. (2019) derived ejection velocities in the range 550–600 km s^{-1}, with one object apparently orbiting counter to the rotation of the galactic disk. For objects with trajectories that place them on unbound orbits,

they should leave the galaxy within (20 kpc)/(500 km s^{-1}) $\approx$ 40 Myr or less. None of our models would fade and contract enough to reach the WD cooling sequence within that amount of time (see Figures 6 and 8), and some even continue to burn He in their cores. For objects that do remain bound to the galaxy, they could eventually cool to form isolated WDs with masses lower than any predicted from single-star evolution.

Due to tidal spin-up of the Roche-lobe filling donor stars, we also expect that the runaway remnants should have significant rotational velocities. Assuming tidal locking, we can estimate the initial rotation period as $P_{rot,0} = P_{orb}$ using values from Table 1. There are then two possibilities that set limits for the observable rotation velocities some time later. In case 1, fluid elements conserve specific angular momentum, so that rotation period at the surface will be $P_{rot} = P_{rot,0} (R/R_0)^2$, where R_0 is evaluated in the initial model at the mass coordinate corresponding to the final bound mass after stripping, which is the fluid element that becomes the new stellar surface. In case 2, we assume that the shear from such a rotation profile would lead to angular momentum transport and rigid rotation, so that total angular momentum conservation in the bound remnant sets the rotation rate. The resulting period is $P_{rot} = P_{rot,0} (I/I_0)$, where $I = \frac{2}{3} \int_0^{M_f} r^2 dm$ is the moment of inertia of the mass that will remain bound after stripping. Table 3 gives surface rotation periods and velocities for these two cases calculated using the MESA models 10 Myr after explosion. Table 3 also includes critical rotation fraction $\Omega_{rot}/\Omega_{crit}$, where $\Omega_{rot} = 2\pi/P_{rot}$ and $\Omega_{crit} = \sqrt{GM/R^3}$. Note that while we have used the profiles from our MESA models to make these estimates for rotational properties, we have not included rotational effects in the MESA models in this work.

We have not addressed the surface compositions of these remnant stars. Clearly, the dominant species within the bulk of the donor star is the unburned helium, with some carbon and oxygen from the earlier core burning. However, after the donor is stripped and still moving within the SN ejecta, it is expected that some of the low-velocity tail of the ejecta will be captured onto the remnant and heavily pollute its surface (Pan et al. 2012b, 2013). Understanding the long-term mixing of these heavy elements in He donor stars may help constrain timescales since explosion for observable objects from this scenario. The opacities from these elements may also influence the thermal evolution timescales as long as they remain near the surface. These topics are left for future work.

The methods applied here are also applicable to modeling binary systems where a WD is the donor star, which can lead to remnants with even higher velocities (Shen et al. 2018a). Equation (3) implies that the high-velocity objects of Shen et al. (2018a) require significant expansion to reach their currently observed radii, while Equation (5) suggests this may

be difficult to explain with shock heating of the donor interior in the WD donor case. We are now exploring this case using `Athena++` and `MESA` models with the appropriate equation of state for degenerate WD interiors.

ORCID iDs

Evan B. Bauer ⓘ https://orcid.org/0000-0002-4791-6724

References

Bauer, E. B., Schwab, J., & Bildsten, L. 2017, ApJ, 845, 97
Bildsten, L., Shen, K. J., Weinberg, N. N., & Nelemans, G. 2007, ApJL, 662, L95
Brooks, J., Bildsten, L., Marchant, P., & Paxton, B. 2015, ApJ, 807, 74
Brown, W. R., Anderson, J., Gnedin, O. Y., et al. 2015, ApJ, 804, 49
De, K., Kasliwal, M. M., Polin, A., et al. 2019, ApJL, 873, L18
Eggleton, P. P. 1983, ApJ, 268, 368
Fink, M., Röpke, F. K., Hillebrandt, W., et al. 2010, A&A, 514, A53
Geier, S., Fürst, F., Ziegerer, E., et al. 2015, Sci, 347, 1126
Geier, S., Marsh, T. R., Wang, B., et al. 2013, A&A, 554, A54
Guillochon, J., Dan, M., Ramirez-Ruiz, E., & Rosswog, S. 2010, ApJL, 709, L64
Hirai, R., Podsiadlowski, P., & Yamada, S. 2018, ApJ, 864, 119
Hirai, R., Sawai, H., & Yamada, S. 2014, ApJ, 792, 66
Hunter, J. D. 2007, CSE, 9, 90
Iben, I., Jr., & Tutukov, A. V. 1991, ApJ, 370, 615
Kasen, D. 2010, ApJ, 708, 1025
Kromer, M., Sim, S. A., Fink, M., et al. 2010, ApJ, 719, 1067
Kupfer, T., van Roestel, J., Brooks, J., et al. 2017, ApJ, 835, 131
Liu, Z.-W., Pakmor, R., Seitenzahl, I. R., et al. 2013, ApJ, 774, 37
Livne, E., & Arnett, D. 1995, ApJ, 452, 62
Marietta, E., Burrows, A., & Fryxell, B. 2000, ApJS, 128, 615
Moll, R., Raskin, C., Kasen, D., & Woosley, S. E. 2014, ApJ, 785, 105
Neunteufel, P., Yoon, S. C., & Langer, N. 2019, A&A, 627, A14
Nomoto, K. 1982, ApJ, 257, 780
Pakmor, R., Kromer, M., Taubenberger, S., & Springel, V. 2013, ApJL, 770, L8
Pan, K.-C., Ricker, P. M., & Taam, R. E. 2010, ApJ, 715, 78
Pan, K.-C., Ricker, P. M., & Taam, R. E. 2012a, ApJ, 760, 21
Pan, K.-C., Ricker, P. M., & Taam, R. E. 2012b, ApJ, 750, 151
Pan, K.-C., Ricker, P. M., & Taam, R. E. 2013, ApJ, 773, 49
Pan, K.-C., Ricker, P. M., & Taam, R. E. 2014, ApJ, 792, 71
Paxton, B., Bildsten, L., Dotter, A., et al. 2011, ApJS, 192, 3
Paxton, B., Cantiello, M., Arras, P., et al. 2013, ApJS, 208, 4
Paxton, B., Marchant, P., Schwab, J., et al. 2015, ApJS, 220, 15
Paxton, B., Schwab, J., Bauer, E. B., et al. 2018, ApJS, 234, 34
Paxton, B., Smolec, R., Schwab, J., et al. 2019, ApJS, 243, 10
Polin, A., Nugent, P., & Kasen, D. 2019, ApJ, 873, 84
Raddi, R., Hollands, M. A., Gänsicke, B. T., et al. 2018a, MNRAS, 479, L96
Raddi, R., Hollands, M. A., Koester, D., et al. 2018b, ApJ, 858, 3
Raddi, R., Hollands, M. A., Koester, D., et al. 2019, MNRAS, 489, 1489
Raskin, C., Scannapieco, E., Fryer, C., Rockefeller, G., & Timmes, F. X. 2012, ApJ, 746, 62
Shen, K. J., Boubert, D., Gänsicke, B. T., et al. 2018a, ApJ, 865, 15
Shen, K. J., Kasen, D., Miles, B. J., & Townsley, D. M. 2018b, ApJ, 854, 52
Sim, S. A., Röpke, F. K., Hillebrandt, W., et al. 2010, ApJL, 714, L52
Taam, R. E., & Fryxell, B. A. 1984, ApJ, 279, 166
Tanikawa, A., Nakasato, N., Sato, Y., et al. 2015, ApJ, 807, 40
Townsley, D. M., Miles, B. J., Shen, K. J., & Kasen, D. 2019, ApJL, 878, L38
van der Walt, S., Colbert, S. C., & Varoquaux, G. 2011, CSE, 13, 22
Vennes, S., Nemeth, P., Kawka, A., et al. 2017, Sci, 357, 680
Wheeler, J. C., Lecar, M., & McKee, C. F. 1975, ApJ, 200, 145
Woosley, S. E., & Kasen, D. 2011, ApJ, 734, 38
Woosley, S. E., & Weaver, T. A. 1994, ApJ, 423, 371
Zhang, M., Fuller, J., Schwab, J., & Foley, R. J. 2019, ApJ, 872, 29